AGU ADVANCING EARTH AND SPACE SCIENCES

Water Resources Research

RESEARCH ARTICLE
10.1029/2023WR034722

Capturing the Dynamic Processes of Porosity Clogging

Mara I. Lönartz[1], Yuankai Yang[1], Guido Deissmann[1], Dirk Bosbach[1], and Jenna Poonoosamy[1]

[1]Institute of Energy and Climate Research – Nuclear Waste Management (IEK-6), Forschungszentrum Jülich GmbH, Jülich, Germany

Key Points:

- Microfluidic experiments to capture precipitation induced porosity clogging under purely diffusive transport conditions
- Isotopic tracer experiments for visualization of solute diffusion through the evolving microporosity of the clogging precipitates
- Validation of modified Archie's law including critical parameters by effective diffusivities derived from experiments and modeling

Supporting Information:

Supporting Information may be found in the online version of this article.

Correspondence to:

M. I. Lönartz,
m.loenartz@fz-juelich.de

Citation:

Lönartz, M. I., Yang, Y., Deissmann, G., Bosbach, D., & Poonoosamy, J. (2023). Capturing the dynamic processes of porosity clogging. *Water Resources Research*, *59*, e2023WR034722. https://doi.org/10.1029/2023WR034722

Received 22 FEB 2023
Accepted 23 OCT 2023

Author Contributions:

Data curation: Mara I. Lönartz
Formal analysis: Mara I. Lönartz
Investigation: Mara I. Lönartz
Methodology: Mara I. Lönartz, Yuankai Yang, Jenna Poonoosamy
Visualization: Mara I. Lönartz
Writing – original draft: Mara I. Lönartz
Writing – review & editing: Mara I. Lönartz, Yuankai Yang, Guido Deissmann, Dirk Bosbach, Jenna Poonoosamy

Abstract Understanding mineral precipitation induced porosity clogging and being able to quantify its non-linear feedback on transport properties is fundamental for predicting the long-term evolution of energy-related subsurface systems. Commonly applied porosity-diffusivity relations used in numerical simulations on the continuum-scale predict the case of clogging as a final state. However, recent experiments and pore-scale modeling investigations suggest dissolution-recrystallization processes causing a non-negligible inherent diffusivity of newly formed precipitates. To verify these processes, we present a novel microfluidic reactor design that combines time-lapse optical microscopy and confocal Raman spectroscopy, providing real-time insights of mineral precipitation induced porosity clogging under purely diffusive transport conditions. Based on 2D optical images, the effective diffusivity was determined as a function of the evolving porous media, using pore-scale modeling. At the clogged state, Raman isotopic tracer experiments were conducted to visualize the transport of deuterium through the evolving microporosity of the precipitates, demonstrating the non-final state of clogging. The evolution of the porosity-diffusivity relationship in response to precipitation reactions shows a behavior deviating from Archie's law. The application of an extended power law improved the description of the evolving porosity-diffusivity, but still neglected post-clogging features. Our innovative combination of microfluidic experiments and pore-scale modeling opens new possibilities to validate and identify relevant pore-scale processes, providing data for upscaling approaches to derive key relationships for continuum-scale reactive transport simulations.

Plain Language Summary Mineral precipitation in porous media alters the pore space geometry and thus affects the transport of fluids and solutes through engineered or geological materials in energy related subsurface systems, used for example, for CO_2 sequestration, utilization of geothermal heat, or geological disposal of radioactive wastes. To understand the long-term evolution of such systems, reactive transport models are employed to simulate transport processes and chemical reactions, coupling changes in porosity and macroscopic transport properties. However, previous studies showed that the effects of localized or widespread pore clogging due to mineral precipitation on diffusive solute transport cannot be captured by the currently used reactive transport models. Here, we conducted microfluidic experiments to resolve the effects of mineral precipitation induced clogging on diffusive solute transport to validate an improved equation coupling porosity and diffusivity (Archie's law). It was shown that an extended version of Archie's law improved the predictability of the transport properties but still neglected reaction processes that occurred after clogging. The combination of microfluidics and pore-scale modeling provides new possibilities to unravel pore-scale processes that potentially need to be considered for further improvement of equations used for macroscopic reactive transport simulations.

1. Introduction

Understanding mineral precipitation induced porosity clogging and quantifying its impact on transport and mechanical properties of porous media is important for several energy-related subsurface systems, including CO_2 sequestration (Brunet et al., 2013; Masoudi et al., 2021; Noiriel et al., 2012; Rathnaweera et al., 2016; Wasch et al., 2013), oil recovery (Schovsbo et al., 2016), geothermal reservoirs (Tranter et al., 2021; Wagner et al., 2005), or deep geological disposal of radioactive waste (De Windt & Spycher, 2019; Fukatsu et al., 2017; Marty et al., 2009; Mon et al., 2017; Samper et al., 2016; Shao et al., 2013; Steefel & Lichtner, 1998; Trinchero et al., 2020; Xie et al., 2022). At the interfaces of multi-barrier systems, chemical and thermal gradients promote mineral precipitation reactions in porous media, altering pore space morphology (pore size, shapes, and connectivity) and porosity of the system. The accompanying reorganization of the flow field can significantly reduce

effective transport properties of the porous media (Chagneau et al., 2015; Hommel et al., 2018; Poonoosamy et al., 2015; Putnis, 2015; Rajyaguru, 2018). As a result, the efficient extraction can be considerably reduced, posing a potential risk on contamination for the surrounding and groundwater resources (De Windt & Spycher, 2019; Marty et al., 2009; Poonoosamy et al., 2015; Seigneur et al., 2019; Tranter et al., 2021; Trinchero et al., 2020; Wagner et al., 2005; Wasch et al., 2013; Xie et al., 2022; Xu et al., 2008). Therefore, a thorough understanding of mineral reaction mechanisms and kinetics in porous media is essential to improve the predictive capability of reactive transport models.

Reactive transport modeling (RTM) has become a versatile tool to assess the long-term evolution of such subsurface systems, coupling geochemical reactions and transport phenomena on different time and length scales. Classical RTM operates at the macroscopic (continuum)-scale, using the concept of the representative elementary volume (REV) (Bear, 1972; Noiriel & Soulaine, 2021; Scheibe et al., 2015). The REV defines the minimum size of a domain over which a property (e.g., porosity) is averaged over a certain length-scale (Bear, 1972). Clogging as a highly localized pore-scale (sub grid) heterogeneity challenges, thus, the predictive capability of continuum-scale RTM using averaged continuous (homogenized) parameters (Chagneau et al., 2015; Deng et al., 2021; Marty et al., 2009; Rajyaguru, 2018; Xie et al., 2015). Because of the inability to describe sub grid changes sufficiently, numerical approaches reveal discretization-dependent results. For instance, Marty et al. (2009) demonstrated how an increasing grid size results in an increase of the predicted time necessary to clog the porosity at a concrete/clay interface. In order to capture effects of clogging at the sub-grid scale, continuum-scale modeling studies employed high-resolution grids, with sizes of the reaction zone smaller than the size of the single grains constituting the porous medium (Katz et al., 2011; Tartakovsky et al., 2008; Xie et al., 2022). Another approach to overcome mesh-discretization dependency at the continuum-scale is employing a hybrid continuum- and pore-scale model, resolving the process of precipitation at the pore-scale (Tartakovsky et al., 2008). Such hybrid (multiscale) models, however, still need an increase in the efficiency of coupling strategies, intending to combine the accuracy of pore-scale models and the computational efficiency of continuum-scale modeling (Battiato et al., 2011; Prasianakis et al., 2020; Scheibe et al., 2015; Tang et al., 2015). This used to be achieved by machine learning techniques with respect to decreasing computational time and interfacing various codes that operate at different length and time scales (Asadi & Beckingham, 2022; D'Elia et al., 2022; Deng et al., 2022; Menke et al., 2021; Prasianakis et al., 2020).

An alternative approach to quantify effective transport properties at the continuum-scale is the development of constitutive equations based on pore-scale modeling results (upscaling) (Deng et al., 2018; Hommel et al., 2018; Menke et al., 2021; Noiriel et al., 2012; Poonoosamy et al., 2020, 2022; Prasianakis et al., 2020; Scheibe et al., 2015; Seigneur et al., 2019). Traditionally, empirical power-law functions are used to parameterize the effective transport properties as a function of porosity, for example, Archie's law (Archie, 1942). Modified versions of these laws also exist considering, in particular, critical minima to capture experimental observations and the expected behavior at the macroscopic scale (Cochepin et al., 2008; Deng et al., 2021; Hommel et al., 2018). There is ample evidence, however, that these empirical relationships are limited in predicting effective transport properties in response to a precipitation induced porosity reduction and pore space changes (Chagneau et al., 2015; Deng et al., 2021; Poonoosamy et al., 2020; Rajyaguru, 2018; Sabo & Beckingham, 2021). With increasing use, the combination of microstructural imaging (e.g., X-ray micro-CT scanning, 3D Raman imaging, positron emission tomography), pore network and pore-scale modeling provide valuable insights for the derivation of extended REV-scale constitutive equations (Agrawal et al., 2021; Kulenkampff et al., 2018; Menke et al., 2021; Noiriel & Soulaine, 2021; Poonoosamy et al., 2022; Roman et al., 2020; Soulaine et al., 2016). However, these extended laws have not been considered in recent modeling approaches, assessing the evolution of barrier interfaces of nuclear waste repositories (Xie et al., 2022) or geothermal systems (Tranter et al., 2021). One possible reason for this might be related to the unknown physical meaning of the added parameters and the difficulties in reliably defining them.

For the specific case of clogging and its impact on the porosity-diffusivity relation, Chagneau et al. (2015) observed a constant non-zero solute flux in response to a celestine precipitation induced porosity reduction and localized clogging. The 1D continuum-scale model based on Archie's law given by $D_e = D_m\, a\, \phi^m$, where D_m is the molecular diffusion coefficient in free water ($m^2\ s^{-1}$) and a and m are empirical fitting parameters either overestimated the amount of precipitates or the diffusive tracer transport, highlighting the need for extensions to classical Archie's law to consider possibly complex precipitation kinetics. Based on a 2D micro-continuum model, Deng et al. (2021) evaluated the effect of different precipitation kinetics and initial pore geometries on the evolving

porosity-diffusivity relationship, extending Archie's law by a critical porosity (ϕ_c) and critical effective diffusivity (D_{ceff}) to account for the effect of pore clogging. The predictive capability of the model was improved, but still existing discrepancies between the numerical results and experimental observations assumed yet undefined pore-scale processes during precipitation induced clogging. As demonstrated by previous column-scale experiments (Rajyaguru, 2018; Tartakovsky et al., 2008) and pore-scale modeling approaches, the complex nature of precipitation processes depends on several factors such as the initial pore geometry (Deng et al., 2021; Noiriel et al., 2016), the reaction rate as a function of supersaturation (Kim et al., 2020; Rajyaguru, 2018; Tartakovsky et al., 2008; Zhang et al., 2010), the probabilistic nature of nucleation (heterogeneous vs. homogeneous) and crystal growth (Deng et al., 2021; Kim et al., 2020; Nooraiepour et al., 2021). The evolving distribution patterns are affected, moreover, by the interplay of local hydrodynamics and reaction kinetics, quantified by the dimensionless Péclet (Pe) and Damköhler (Da) numbers (Battiato et al., 2011; Poonoosamy et al., 2019; Seigneur et al., 2019; Tartakovsky et al., 2008). The Pe is defined locally as: $\mathrm{Pe} = uL^*/D_m$, where u is the fluid velocity (m s^{-1}), and L^* is a characteristic length (m), at the pore-scale, typically the average grain size (Seigneur et al., 2019; Soulaine et al., 2017; Steefel et al., 2013). The Da for diffusive systems is defined as $\mathrm{Da}_{\mathrm{II}} = (L^{*2}/D_e)/(c/r)$, where D_e is the effective diffusion coefficient in free water ($m^2\ s^{-1}$), c is the equilibrium concentration (mol kg_{water}^{-1}) and r is the reaction rate (mol $kg_{water}^{-1} s^{-1}$) (Steefel et al., 2013). In addition, the Reynolds number $\mathrm{Re} = uL^*/\nu$, with ν as the kinematic viscosity ($m^2\ s^{-1}$) is used to describe the ratio between inertial and viscous forces (Steefel et al., 2013). However, all these aforementioned constraints challenge recent pore-scale modeling approaches that aim to predict precipitation processes, highlighting the need for further experimental studies to overcome limitations in the spatial and temporal resolution of the applied 2D/3D imaging techniques (Noiriel & Soulaine, 2021).

In this study, we provide new insights into mineral precipitation induced porosity clogging and its effect on the porosity-diffusivity relationship, combining innovative microfluidic experiments with pore-scale modeling. The experimental setup follows our previous concept proposed by Poonoosamy et al. (2019, 2021). The design of the microfluidic reactor allowed a real-time monitoring of precipitation-dissolution reactions under purely diffusive transport conditions in a quasi two-dimensional porous medium. The chemical system as well as the geometry of the microfluidic reactor were chosen in consideration of the work of Chagneau et al. (2015) and Deng et al. (2021). Based on the time-lapse optical images, simulations were performed to determine the effective diffusivity as a function of the evolving porous media, using pore-scale modeling. The diffusive transport of stable isotopes through the evolving porous medium was traced by Raman spectroscopy. The combination of time-lapse optical microscopy and confocal Raman spectroscopy opens up new possibilities to decipher pore-scale processes without the need of disturbing reaction and flow field conditions, overcoming limitations in the spatial and temporal resolution of typical flow cell or column-scale experiments (Chagneau et al., 2015; Katz et al., 2011; A. Tartakovsky et al., 2008) and providing data for upscaling parameters to derive key relationships for continuum-scale RTM.

2. Materials and Methods

2.1. Experimental Setup and Microreactor Design

The experimental setup combines a microfluidic device with high-resolution time-lapse optical microscopy and confocal Raman spectroscopy. The microfluidic reactor consists of a porous reaction chamber with dimensions of 100 × 66 × 1 µm³, referred to as quasi two-dimensional region of interest (ROI). The uniform distribution of cylindrical pillars (grains) of 10 µm in diameter distanced by 1 µm create a fully connected pore network with an initial porosity, ϕ_i, of 0.36 (Figures 1b and 1c). The porous reaction chamber is connected to 10-µm deep supply channels via small inlets of 20 × 3 × 1 μm^3 on each side (Figure 1c).

The microreactor was mounted on an automatically moving x-y-z stage of the inverted microscope and connected to a syringe pump (NeMeSYS, Cetoni GmbH, Korbußen, Germany) (Figure 1a). The single-use polydimethylsiloxane (PDMS)-glass reactor was fabricated following the procedure from Poonoosamy et al. (2019) and references therein. Before the experiment, the reactor was purged with MilliQ water for 1 hr. The solutions of 0.05 M strontium chloride ($SrCl_2$) and sodium sulfate (Na_2SO_4) were filtered with sterile Millex-GP syringe filter units (0.22 µm pore size) to remove solid particles and bacteria that may be present. The solutions were, then, injected with a constant flow rate of 1,000 nL min^{-1} into the microreactor to trigger a diffusion-driven precipitation of celestine ($SrSO_4$) inside the porous reaction chamber as follows:

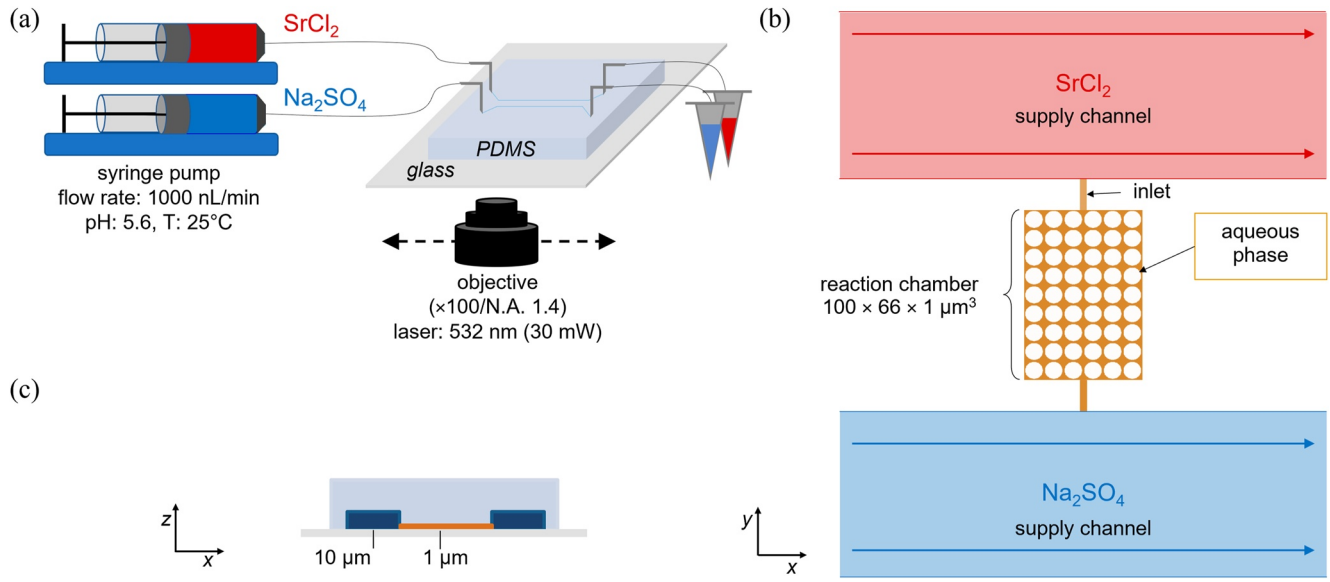

Figure 1. Microfluidic experimental setup for precipitation induced clogging experiments monitored by time-lapse optical microscopy and confocal Raman spectroscopy. (a) PDMS-glass chip mounted on the automatically moving x-y-z stage for time-lapse optical imaging and Raman imaging. (b) Top and (c) Cross-sectional view of the microfluidic reactor.

$$Sr^{2+}_{(aq)} + SO^{2-}_{4(aq)} \rightarrow SrSO_{4(s)}$$

The experiments were conducted at room temperature (22°C). Post-porosity clogging, a deuterated solution of $SrCl_2$ was injected to monitor the transport of D_2O by Raman imaging. Deuterium oxide was chosen as a stable isotope tracer, here, as a hydrogen isotopic Raman tracer. The experiment was duplicated (Exp1 and Exp2).

2.2. Time-Lapse Optical Microscopy and Confocal Raman Spectroscopy

The microfluidic experiments were conducted with a Witec alpha300 Ri Inverted Confocal Raman Microscope, equipped with 100× oil immersion objective with a numerical aperture (NA) of 1.4, a working distance of 0.16 mm and a cover glass correction for 0.17 mm. The resolution of the microscope was estimated to be $0.6 \times 0.6 \times 1$ µm^3; (voxel resolution – 0.3 µm). Bright field images with a resolution of 6.85 pixel µm^{-1} were taken every 15 and 10 min, respectively, to monitor the evolving pore space geometry at regular time intervals. The amount of celestine was measured by segmenting and thresholding the optical images using the open-source software Fiji (Schindelin et al., 2012), allowing the derivation of the crystal growth rate (mol s^{-1}), precipitation rate (mol m^2 s^{-1}) and porosity (−) as a function of time. The 2D images were segmented into three phases (PDMS, aqueous phase, celestine), serving as input files for the pore-scale simulations by using the *TauFactor* Matlab application created by Cooper et al. (2016).

All Raman spectroscopic measurements were performed with a Nd:YAG laser (λ = 532 nm). The scattered light was dispersed by a grating of 600 grooves mm^{-1} of the Ultra-High-Throughput Spectrometer UHTS300 and detected by a thermoelectrically cooled CCD Camera. The usage of a 100× oil immersion objective yielded a theoretical diffraction-limited lateral and axial resolution of 464 nm ($d_x = \frac{1.4\lambda}{NA}$) and 1,629 nm ($d_z = \frac{4n\lambda}{NA^2}$), considering a refraction index (n) of 1.5 for the glass cover lid of the reactor (Everall, 2010). The spectral resolution was ~3.5 cm^{-1}. To avoid a potential heating of the microfluidic reactor, the laser power was set to 40 mW and an integration time of 0.25 s was chosen, resulting in a maximum output power of 0.5 mW. The output laser power was controlled by a handheld Laser Power Meter from Coherent before the experiments. The transport of D_2O as a chemically "inert" and Raman active tracer was visualized by large area scans (115×75 µm^2) including the entire ROI (100×66 µm^2) with a step size of 1 µm. At each step, a Raman spectrum was recorded in the wavenumber range between 200 and 3,950 cm^{-1} to detect all representative Raman modes of celestine, deuterium and water. Further details about Raman mode assignment and data

treatment are given in Supporting Information S1. As the spatial resolution of the optical and Raman spectroscopic microscopy is above the depth of the porous reaction chamber, the region of interest displays a quasi two-dimensional system.

2.3. Modeling of Initial Velocity and Concentration Field

The initial transport velocity and solute concentration fields were modeled across the 3D microfluidic reactor at steady state using the software COMSOL Multiphysics 6.0 (COMSOL AB, Stockholm, Sweden). The conditions of mass transport were assessed in terms of the dimensionless Reynolds (Re) and Pe numbers (Equations S4 and S5 in Supporting Information S1). The Re was calculated for the supply channels using a characteristic length of 3×10^{-4} m corresponding to the total lengths of the supply channels. The Pe was calculated for the ROI with a characteristic length of 1×10^{-5} m corresponding to the diameter of the cylindrical pillars referred to as the average grain size. The diffusion coefficients were set to 1.23×10^{-9} m^2 s^{-1} for Na_2SO_4, and 1.34×10^{-9} m^2 s^{-1} for $SrCl_2$, representing the diffusion coefficients of the respective salt solution, D_{salt} (Equation S3 in Supporting Information S1; Lasaga, 1979). For the derivation of the theoretical maximum saturation index (SI), the species activities at the theoretical maximum concentration of $SrCl_2$ and Na_2SO_4 were calculated with GEM-Selektor V3.42. Further details can be found in Text S2 and S4 in Supporting Information S1.

2.4. Simulation of Tracer Diffusion by Pore-Scale Modeling

The effective diffusivities as a function of the evolving pore geometry were calculated by using the MatLab application *TauFactor* (Cooper et al., 2016) based on the 2D segmented images. The diffusion equation in the porous medium domains for non-charged species is given by:

$$\frac{\partial C_p}{\partial t} = \nabla \cdot (D_0 \nabla C_p) \tag{1}$$

with C_p as the local concentration of the inert tracer at the pore-scale and D_0 as the local diffusion coefficient of the tracer in pure water. The constant concentrations (C_{in} and C_{out}) at inlet and outlet are employed as the boundary conditions. At steady state, Equation 1 reduces to the Laplace equation. The effective diffusion coefficient, D_e (m^2 s^{-1}), was then calculated with the total mass flux J obtained at the steady state for the entire porous reaction chamber:

$$D_e = \frac{J \cdot L}{S(C_{in} - C_{out})} \tag{2}$$

with $L = 100$ µm as the respective length of the ROI and $S = 66 \times 1$ µm^2 as the total cross-sectional area.

For the clogged state, the concentration evolution with time was numerically solved by including a diffusivity of D_2O in the precipitate, also named as the critical effective diffusivity, D_{ceff} (m^2 s^{-1}). D_{ceff} (m^2 s^{-1}) was determined by fitting with the experimentally determined time of diffusion, t_{diff}, considering a minimum and maximum microporosity of 0.01 and 0.05, respectively, of the clogging precipitates.

3. Results

3.1. Modeling of Initial Velocity and Concentration Fields

The transport velocity and the distribution of the $SrCl_2$ and Na_2SO_4 concentrations for the non-reactive (initial) steady state of the 3D microfluidic reactor (i.e., before celestine precipitation occurred) were simulated, using COMSOL Multiphysics. The averaged velocity of 2.67×10^{-2} m s^{-1} along the supply channels with a characteristic length of 3.00×10^{-4} m yields a Re number of 8.02, ensuring a laminar flow and advective transport of reactants at a constant rate inside the supply channels. From the laminar flow regime inside the channels through the 1 µm-deep inlets toward the center of the porous reaction chamber, the average velocity significantly decreases by six orders of magnitudes. Inside the chamber, the simulation yields a maximum velocity of 8.87×10^{-6} m s^{-1}, leading to a Pe number significantly below <0.1 and thus, indicating a purely diffusive transport of reactants within the porous reaction chamber. The distribution of Na_2SO_4 and $SrCl_2$ concentrations within the supply channels shows a constant behavior, according to the laminar flow field (Figure 2a). Based on the concentration profiles of Na_2SO_4 and $SrCl_2$, a diffusive mixing of the reactants is expected to occur at a theoretical concentration of 25 mM, yielding a saturation index for celestine of 2.14 at the center of the reaction chamber (Figure 2b).

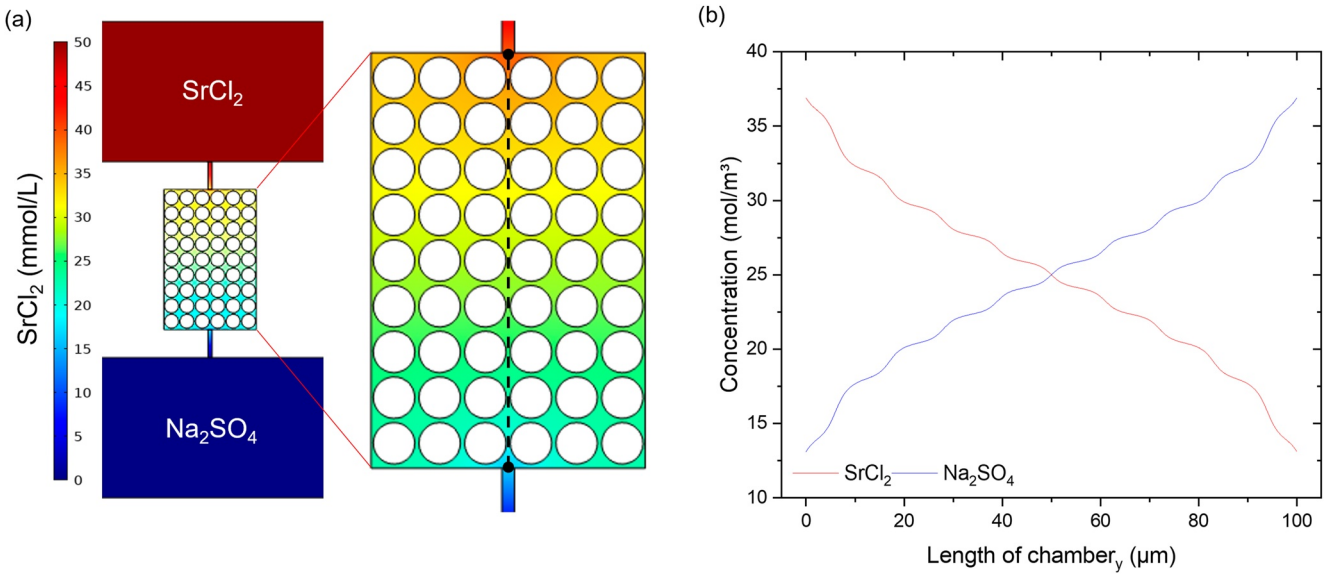

Figure 2. Simulated (a) concentration field of $SrCl_2$ at steady-state displayed as mid-plane at $z = 0.5$ µm of the microfluidic reactor. The dashed line marks the position of the concentration profiles shown in (b).

3.2. Experimental Evaluation of Mineral Reactions and Porosity

Figure 3 shows the evolving porous media in response to celestine precipitation induced clogging for Exp1 and Exp2. The processes can be subdivided into five stages: (a) induction time, preceding the appearance of the first crystallite, (b) crystal growth, (c) clogging, (d) dissolution, and (e) precipitation (Figure 4). Both experiments showed similar induction times and growth rates (2.0×10^{-15}, 2.4×10^{-15} mol s^{-1}), describing a sigmoidal (logistic) growth function. The precipitation of celestine started within the center of the reactor ($y = 50$ µm), where the supersaturation with respect to celestine reaches a theoretical maximum of 2.14. However, the different locations in x-direction of the first occurring crystallites can be linked to the probabilistic nature of nucleation (Agarwal & Peters, 2014; Prieto, 2014), and initial defects on the surface of the chip. The flat euhedral celestine crystallites show a preferred direction of growth toward the incoming SO_4^{2-}. The growth rates were normalized to the reactive surface area, yielding initial precipitation rates of 8.90×10^{-5} and 8.21×10^{-6} mol m^2 s^{-1} that decreased to 2.8×10^{-5} and to 2.4×10^{-5} mol m^2 s^{-1}, respectively, until the porous reaction chambers became clogged, stopping further precipitation reactions. The precipitation rates averaged over time until clogging yielded an estimated Damköhler number of ~22 (cf. Equation S6 in Supporting Information S1). At the clogged state, however, the initial porosity of 0.36 decreased to a minimum porosity of 0.29 and 0.26, respectively, referred to as the critical porosity, ϕ_c. For Exp1, first signs of dissolution were noted after 18 ± 7 min of clogging, showing a relatively fast dissolution of the crystal surface facing the SO_4^{2-} inlet (red arrow in Figure 3a). The dissolving crystal surface partially reopened the disconnected porosity, providing further sulfate from the dissolving phase itself and via the SO_4^{2-} inlet. The post-clogging crystal growth decreased the critical porosity to 0.27, reaching the same value as observed for Exp2. In the case of Exp2, however, the state of clogging lasted significantly longer, showing first signs of dissolution after 115 ± 5 min of clogging along both sides of the precipitation front. In addition, the formation of a non-uniform microporosity of celestine was observed, indicating the evolution of a diffusivity of the clogging precipitates (blue arrows in Figure 3b). In the diffusion-controlled reaction chamber (low Pe), local precipitation along the dissolving crystal surfaces presumably lead to a second state of clogging. However, limitations in the spatial resolution did not allow to further define post-clogging reaction mechanisms and rates (kinetics) and to resolve the temporal evolution of the celestine microporosity.

3.3. Experimental Evaluation of the Critical Effective Diffusivity

As the pore network became microscopically clogged, a deuterated 0.05 M $SrCl_2$ solution was injected in the respective supply channel to monitor the transport of D_2O through the evolving porous media using 2D Raman imaging. Figure 5 shows Raman distribution images of deuterium and celestine for Exp1 and Exp2 at two

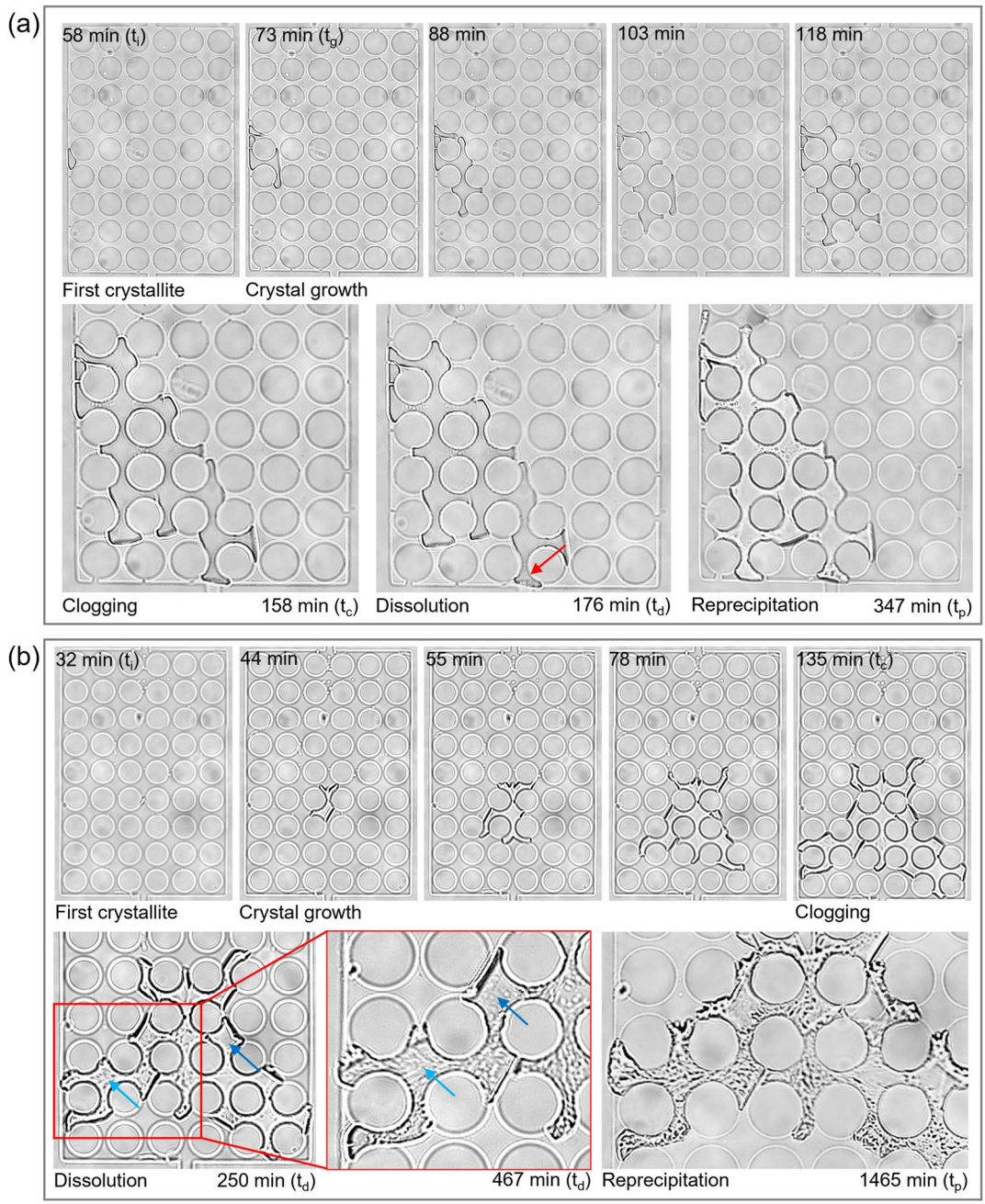

Figure 3. Time-lapse bright field images representative for the five process stages of (a) Exp1 and (b) Exp2 (cf. Movies S1 and S2). The red arrow points to the dissolving crystal surface at the SO_4^{2-} inlet. The light blue arrows mark the evolving high microporosity of celestine. The dark blue arrows point to low microporosity areas of the crystal. t_i: induction time; t_g: crystal growth; t_c: clogging; t_d: dissolution, t_p: precipitation.

different time steps, t_0 and t_{diff}. The stacked Raman spectra were obtained from the pore solution averaged over different areas labeled as A, B and C. At t_0, deuterium is diffusing into the reaction chamber via the $SrCl_2$-inlet (blue rectangle, spectrum A in Figure 5), whereby the pore solution within the disconnected porosity showed no detectable D_2O (green rectangle, spectrum B in Figure 5). For Exp1, the first Raman signals of D_2O diffused trough the clogging precipitates were detected after ~2.93 hr (red spectrum C in Figure 5a). In the case of Exp2, the transport of deuterium through the evolving microporosity of the clogging precipitate took about 17.3 hr (red spectrum C in Figure 5b). The observed significant difference in the time of diffusion is attributed to the non-uniformly developing microporosity of the precipitate (cf. Section 3.2, Figure 3b-t_d). Both tracer

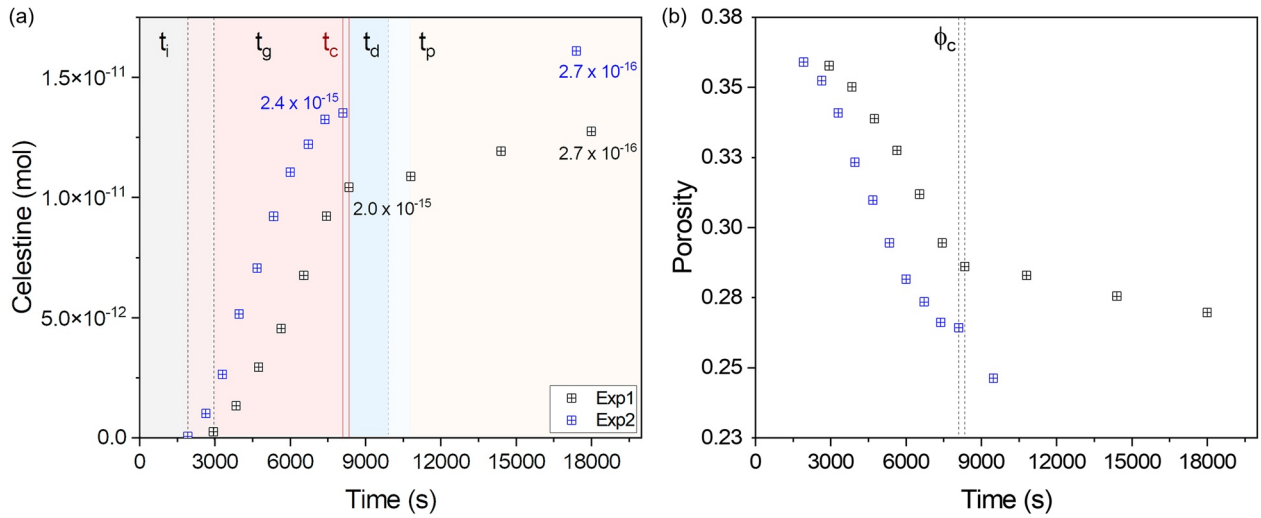

Figure 4. (a) Amount of celestine as a function of time for Exp1 (black squares) and Exp2 (blue squares). The given numbers represent the crystal growth rates (mol s^{-1}) obtained from a linear fit over t_g–t_c, and t_c–t_p. (b) Porosity as a function of time until reaching the critical porosity, ϕ_c, at the clogged state (dashed line).

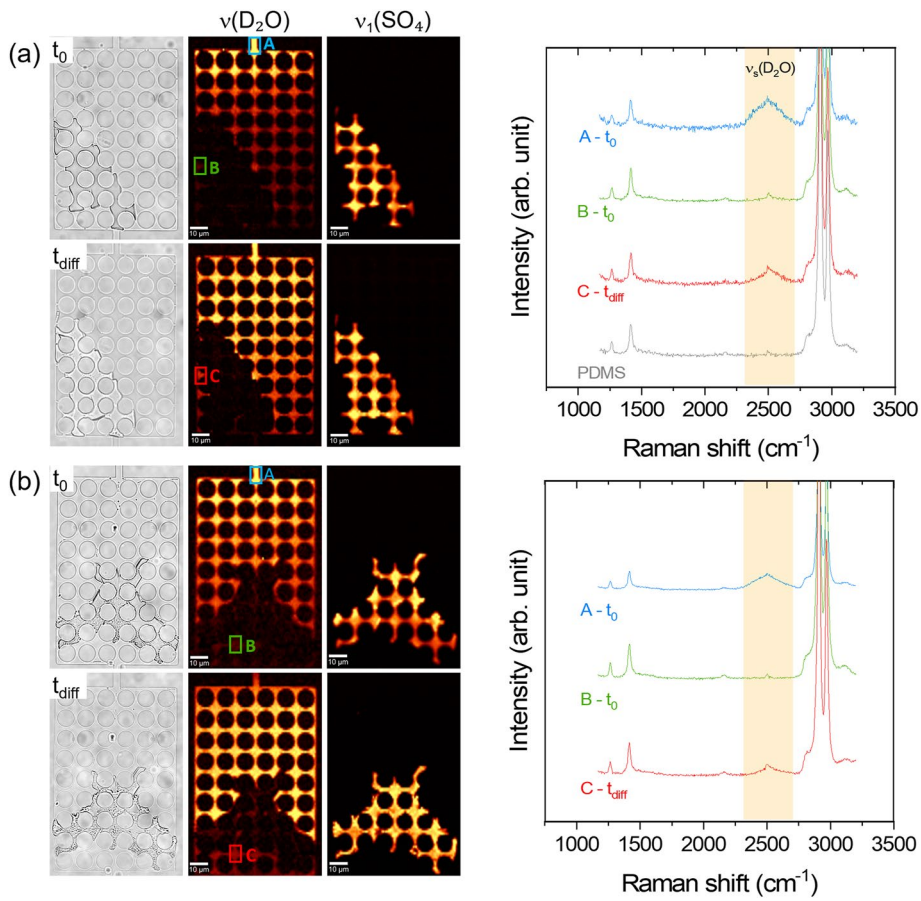

Figure 5. Raman images of the $\nu_s(D_2O)$ and $\nu_1(SO_4)$ intensities during clogging at t_0 and the time of D_2O diffusion (t_{diff}) for (a) Exp1 and (b) Exp2. The blue, green and red rectangles mark the location of the averaged Raman spectra (right side): A, incoming deuterated $SrCl_2$ solution at t_0; B, D_2O-free pore solution at t_0; C, pore solution at t_{diff}. The PDMS spectrum (light gray) serves as reference for intensity.

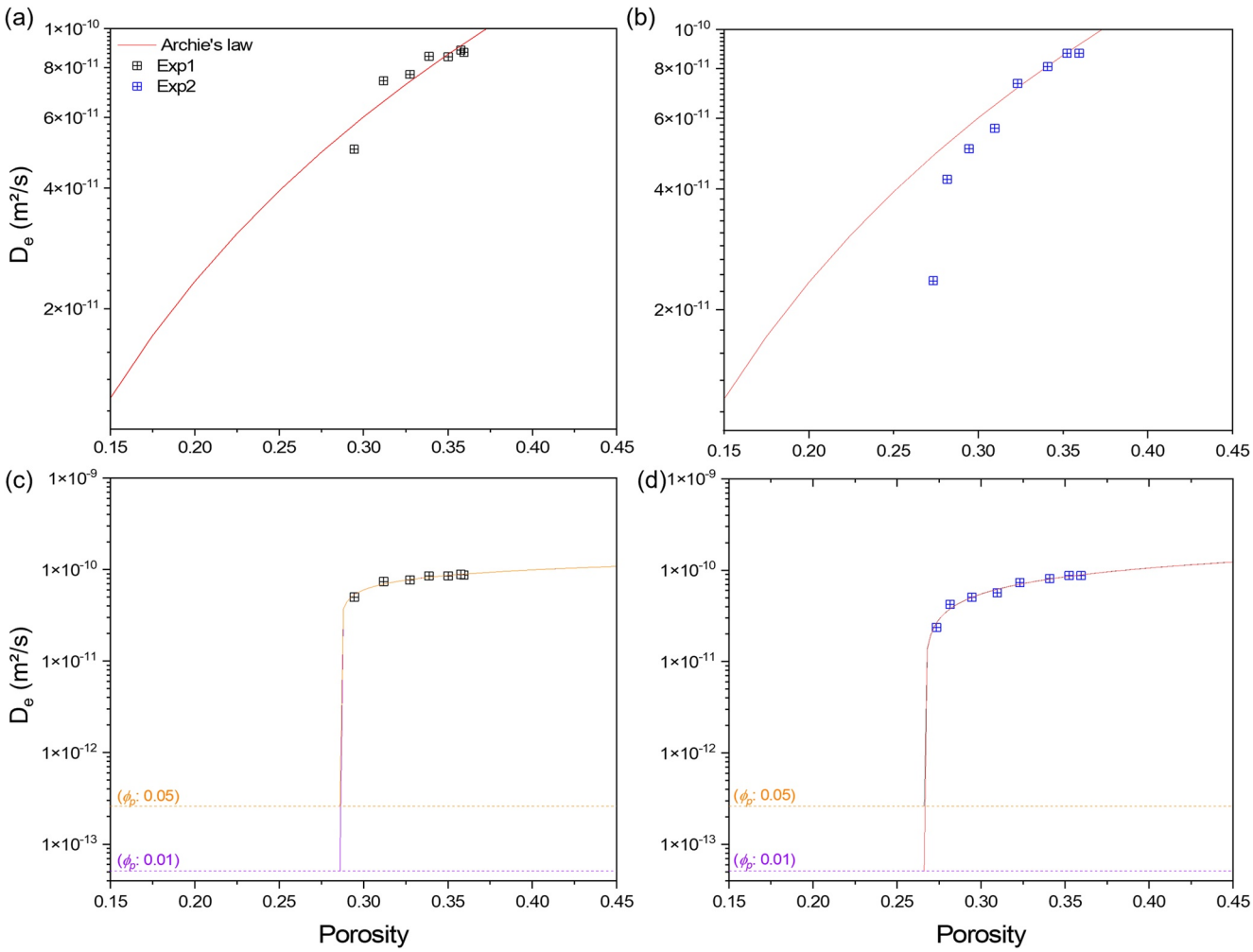

Figure 6. Simulated effective diffusivity as a function of decreasing porosity for (a) Exp1 (black squares) and (b) Exp2 (blue squares) calculated with TauFactor. The red curves represent Archie's law. (c)–(d) The extended law considering a minimum (5.1×10^{-14} m^2 s^{-1}, purple curve) and maximum (2.6×10^{-13} m^2 s^{-1}, orange curve) D_{ceff}.

experiments, however, capture the diffusive transport of molecular water through the evolving microporosity of the precipitates. The diffusivity of the precipitates itself is referred to as the critical effective diffusivity, D_{ceff}. To estimate the D_{ceff}, a sensitivity analysis was performed by assuming a minimum and maximum microporosity of 0.01 and 0.05 of the clogging celestine (cf. Section 2.4). The study yielded critical effective diffusivities in the range from 5.1×10^{-14} to 2.6×10^{-13} m^2 s^{-1}.

3.4. Numerical Evaluation of the Effective Diffusivity

The 2D optical images shown in Section 3.2 were segmented into three phases (i.e., solid phase (initial porous medium), aqueous phase, and celestine precipitates) and used as input files to calculate the effective diffusivity for every time step, using the Matlab application *TauFactor* (see Text S5 in Supporting Information S1). Figure 6 displays the effective diffusivities as a function of decreasing porosity. The initial effective diffusivity of 8.72×10^{-11} decreases to 5.00×10^{-11} m^2 s^{-1} and 2.36×10^{-11} m^2 s^{-1}, respectively, in Exp1 and Exp2 before reaching critical porosity at the clogged state. The difference in the evolution of the porosity–diffusivity observed for Exp1 and Exp2 is related to the distinctly evolving pore space morphology, leading to different effective diffusivities by the same reduction of porosity. However, Archie's law fails to describe the porosity–diffusivity relationship in response to mineral precipitation reactions, increasingly deviating from the simulated diffusivities

toward clogging. Therefore, an extended version of Archie's law proposed by Deng et al. (2021) was tested to explicitly account for the case of clogging as follows:

$$D_e = D_{ceff} + aD_m(\phi - \phi_c)^n \quad (3)$$

whereby a and n represent empirical coefficients (Sahimi, 1994). D_m is set to 1×10^{-9} m^2 s^{-1} as molecular diffusion coefficient. The minimum porosity reached during clogging is defined as the critical porosity, ϕ_c. D_{ceff} represents the critical effective diffusivity of the clogged porous medium. In the pore-scale modeling approach from Deng et al. (2021), no direct measurement of this parameter was performed and two values (5×10^{-12}, 1×10^{-15} m^2 s^{-1}) were tested to reproduce the experimental tracer flux at the continuum-scale provided by Chagneau et al. (2015). In this study, therefore, the D_{ceff} was estimated based on the Raman tracer experiments, yielding 5.1×10^{-14} and 2.6×10^{-13} m^2 s^{-1} within the range given by Deng et al. (2021) (cf. Section 3.3). The application of the extended law (ϕ_c-D_{ceff}) improves the description of the evolving effective diffusivity in response to mineral precipitation reactions using the experimentally determined critical parameters (Figures 6c and 6d). However, the extended version does not consider post-clogging features with respect to a further evolving critical effective diffusivity.

4. Discussion

4.1. The Non-Final State of Clogging

The microfluidic experiments of mineral precipitation induced porosity-clogging demonstrated the non-final state of clogging, showing a diffusive transport of molecular water through the evolving microporosity of celestine and a non-linear feedback on post-clogging reaction rates and porosity. Under diffusive transport conditions (low Pe numbers), the probabilistic nature of nucleation as well as the different diffusion coefficients of the dissolved reactants governed the final distribution of the clogging precipitates. The pattern of a uniform precipitation front perpendicular to the direction of diffusion as observed in Exp2 has also been described for column-scale experiments (Chagneau et al., 2015; Rajyaguru, 2018) and captured by pore-scale models (Deng et al., 2021; Tartakovsky et al., 2008). However, common setups used for diffusion-driven precipitation experiments do not allow the in situ observation of post-clogging reactions and thus, only a few pore-scale modeling approaches assumed dissolution as a post-clogging process, maintaining quasi-equilibrium chemical conditions near the precipitation zone (Tartakovsky et al., 2008). The microfluidic experiments clearly showed dissolution reactions as a post-clogging feature, occurring along the outer sides of the precipitation front due to a limited transport of reactants and causing the development of a microporosity in the precipitates. Raman tracer experiments qualitatively confirmed the assumed diffusivity of the precipitated phase, providing one explanation for the non-zero flux and its increase over time as reported from Chagneau et al. (2015). At this point, however, it should be noted that the microporosity and its temporal evolution could not be resolved, raising the question how the initial nano- to micro-porosity of the clogging precipitates controls the (critical) effective diffusivity. On the one hand, it is most likely that further precipitation in the microporous crystalline phase is inhibited due to the pore-size controlled solubility (PCS) effect (Emmanuel & Ague, 2009) or kinetic effect (Churakov & Prasianakis, 2018; Poonoosamy et al., 2016). The PCS effect could explain, in fact, the diffusive transport of deuterium through the clogging precipitates and the post-clogging precipitation reactions along dissolving crystal surfaces as clearly demonstrated in this study, confirming Deng et al.'s (2021) assumptions.

4.2. Simulated Porosity-Diffusivity Relation in Response to Clogging

Archie's law became inadequate to predict the porosity-diffusivity evolution in response to a significant porosity decrease, showing a deviant behavior in comparison to the simulated effective diffusivities. Similar observations were reported for diffusion-driven precipitation experiments at the column-scale (Chagneau et al., 2015; Rajyaguru, 2018) and in microfluidic experiment (Poonoosamy et al., 2022), demonstrating how a simple power law function underestimates the effect of a localized porosity reduction (Chagneau et al., 2015; Deng et al., 2018; Hommel et al., 2018; Poonoosamy et al., 2022; Rajyaguru, 2018). The differences in the evolution of the porosity-diffusivity evolution observed in this study can be ascribed to different locations of nucleation and crystal growth, resulting in distinct changes in the flow pathways and thus, in the effective diffusivity at the same reduction of porosity. Tartakovsky et al. (2007) reported similar observations for a pore-scale reactive

transport model, demonstrating that the flux decreases less if the precipitation is uniform than if precipitation is non-uniform.

The extended version of Archie's law improved the description of the evolving effective diffusivity toward porosity clogging, considering a critical porosity and a critical effective diffusivity. The time-lapse optical images allowed an easy determination of the critical porosity, ϕ_c, without disturbing or interrupting ongoing reaction and transport processes. In this context, a further decrease in the ϕ_c could be observed during Exp1. Due to the ongoing post-clogging reactions, a reliable determination of a critical effective diffusivity referring to the total respective porous medium turned out to be challenging. Nevertheless, the estimated results were within the range of the assumed values from Deng et al. (2021) and showed a significant decrease in the effective diffusivity by two to three orders of magnitudes for a relatively low porosity reduction of 25%. Interestingly, this behavior is also predicted by various porosity-permeability relationships as reviewed in the work from Hommel et al. (2018).

In recent continuum and pore-scale modeling approaches, however, porosity clogging is often predicted as a final state at which the molecular diffusion of water stops after reaching a critical porosity that goes to zero or is set to <1% for numerical reasons, neglecting experimentally observed non-zero fluxes (Chagneau et al., 2015; Deng et al., 2021; Marty et al., 2009; Wasch et al., 2013; Xu et al., 2004). For instance, Deng et al. (2021) performed numerical tracer experiments on a 2D computational domain of similar size as the microfluidic reaction chamber, showing no break-through of the tracer after 10 million seconds (115.7 days) of clogging and ignoring dissolution as a post-clogging phenomenon. In this study, the diffusive transport through the precipitates was qualitatively approved after approximately 18 min and 2 hr of clogging, respectively, for Exp1 and Exp2, revealing significant differences in the time of diffusion due to the non-uniform evolution of the microporosity of the clogging precipitates. Deng et al. (2021) suggested a broad applicability of the extended law for 3D systems. Based on the work of Hunt (2004), a larger fitting exponent, m, of traditional Archie's law for 3D systems compared to 2D systems is to be expected. Here, our aim was particularly to experimentally validate the extended law proposed by Deng et al. (2021) and to determine the critical parameters (D_{ceff}, ϕ_c) for a well-defined system. For extension to full 3D systems, further studies are needed to reliably evaluate the proposed critical parameters due to the related increase in complexity, for example, in pore space geometry. However, it is presumed that the fundamental formulation of the extended power law remains unchanged.

Future work needs, thus, to focus on the effects of different distribution patterns on the evolving effective diffusivity toward clogging, considering different initial geometries, minerals (crystal habit) and Da numbers, and, second, the effect of nano- to micro-porosity of the precipitates on the post-clogging evolution of the reactive porous medium using more advanced analytical techniques with higher spatial resolution, for example, FIB-SEM or FIB tomography. Additionally, the authors propose to conduct systematically sensitivity analysis using the extended law (Equation 3) for modeling subsurface evolution.

5. Conclusion

The microfluidic experiments of mineral precipitation induced porosity-clogging demonstrated the non-final state of clogging, showing a diffusive transport of molecular water through the evolving microporosity of celestine and a non-linear feedback on post-clogging reaction rates and porosity changes. The post-clogging dissolution reactions provided one explanation for the experimentally observed non-zero fluxes and its increase over time. The non-uniform evolution of a microporosity of the clogging precipitates challenged the determination of a critical effective diffusivity. However, the estimated values predicted a significant decrease in the effective diffusivity by two to three orders of magnitude by a total porosity reduction of 25%. The diffusivity of the clogging precipitates resulted in localized precipitation, potentially reclogging the porous media. Archie's law failed to describe the porosity-diffusivity relationship in response to mineral precipitation reactions, increasingly deviating from the simulated diffusivities toward clogging. The extended version of Archie's law proposed by Deng et al. (2021) was tested to explicitly account for the case of clogging. The extended law considering a critical porosity and a critical effective diffusivity improved the prediction of the porosity–diffusivity evolution in response to mineral precipitation induced clogging. However, post-clogging features are still not considered. Therefore, future pore-scale modeling approaches and microfluidic experiments are required to systematically assess the effect of a microporosity on the effective diffusivity, providing further data for upscaling approaches to derive key relationships for continuum-scale reactive transport simulations. Future work foresees three-dimensional microfluidic experiments under more realistic conditions, assessing different initial pore geometries and ranges of porosities.

Data Availability Statement

The segmented optical images of Exp1 and Exp2 used as input data for calculating the effective diffusivity with the *TauFactor* Matlab application (Cooper et al., 2016) can be accessed under http://doi.org/10.34730/b0a7e1f3d-7484d84ace8d5d83f931e94. The files also contain the COMSOL Multiphysics project file, the raw Raman data set and the output data from the with GEM-Selektor V3.42 used to calculate the saturation index. In addition, the amount of celestine, porosity and the calculated effective diffusivities as function of time are given.

Acknowledgments
The research leading to these results has received funding from the German Federal Ministry of Education and Research (BMBF) under grant agreement No. 02NUK053A and Innovation and Networking Fund of the Helmholtz-Association (Grant SO-093) within the iCross project. This research has also received funding from the European Union's Horizon 2020 research and innovation program under grant agreement No. 847593 (EURAD) within work package DONUT. We thank Kathy Dahmen for technical support. M.I.L thanks Gerrit Müller for fruitful discussions and comments. Open Access funding enabled and organized by Projekt DEAL.

References

Agarwal, V., & Peters, B. (2014). Solute precipitate nucleation: A review of theory and simulation advances. In *Advances in chemical physics: Volume 155* (pp. 97–160). John Wiley & Sons, Ltd. https://doi.org/10.1002/9781118755815.ch03

Agrawal, P., Mascini, A., Bultreys, T., Aslannejad, H., Wolthers, M., Cnudde, V., et al. (2021). The impact of pore-throat shape evolution during dissolution on carbonate rock permeability: Pore network modeling and experiments. *Advances in Water Resources*, *155*, 103991. https://doi.org/10.1016/j.advwatres.2021.103991

Archie, G. E. (1942). The electrical resistivity log as an aid in determining some reservoir characteristics. *Transactions of the AIME*, *146*(01), 54–62. https://doi.org/10.2118/942054-G

Asadi, P., & Beckingham, L. E. (2022). Intelligent framework for mineral segmentation and fluid-accessible surface area analysis in scanning electron microscopy. *Applied Geochemistry*, *143*, 105387. https://doi.org/10.1016/j.apgeochem.2022.105387

Battiato, I., Tartakovsky, D. M., Tartakovsky, A. M., & Scheibe, T. D. (2011). Hybrid models of reactive transport in porous and fractured media. *Advances in Water Resources*, *34*(9), 1140–1150. https://doi.org/10.1016/j.advwatres.2011.01.012

Bear, J. (1972). *Dynamics of fluids in porous media* (p. 764). American Elsevier Publishing Company.

Brunet, J. P. L., Li, L., Karpyn, Z. T., Kutchko, B. G., Strazisar, B., & Bromhal, G. (2013). Dynamic evolution of cement composition and transport properties under conditions relevant to geological carbon sequestration. *Energy & Fuels*, *27*(8), 4208–4220. https://doi.org/10.1021/ef302023v

Chagneau, A., Claret, F., Enzmann, F., Kersten, M., Heck, S., Madé, B., & Schäfer, T. (2015). Mineral precipitation-induced porosity reduction and its effect on transport parameters in diffusion-controlled porous media. *Geochemical Transactions*, *16*(1), 13. https://doi.org/10.1186/s12932-015-0027-z

Churakov, S. V., & Prasianakis, N. I. (2018). Review of the current status and challenges for a holistic process-based description of mass transport and mineral reactivity in porous media. *American Journal of Science*, *318*(9), 921–948. https://doi.org/10.2475/09.2018.03

Cochepin, B., Trotignon, L., Bildstein, O., Steefel, C. I., Lagneau, V., & Van der Lee, J. (2008). Approaches to modelling coupled flow and reaction in a 2D cementation experiment. *Advances in Water Resources*, *31*(12), 1540–1551. https://doi.org/10.1016/j.advwatres.2008.05.007

Cooper, S. J., Bertei, A., Shearing, P. R., Kilner, J. A., & Brandon, N. P. (2016). TauFactor: An open-source application for calculating tortuosity factors from tomographic data. *SoftwareX*, *5*, 203–210. https://doi.org/10.1016/j.softx.2016.09.002

D'Elia, M., Deng, H., Fraces, C., Garikipati, K., Graham-Brady, L., Howard, A., et al. (2022). Machine learning in heterogeneous porous materials. *AmeriMech Symposium Series*. https://doi.org/10.48550/arXiv.2202.04137

Deng, H., Molins, S., Trebotich, D., Steefel, C., & DePaolo, D. (2018). Pore-scale numerical investigation of the impacts of surface roughness: Upscaling of reaction rates in rough fractures. *Geochimica et Cosmochimica Acta*, *239*, 374–389. https://doi.org/10.1016/j.gca.2018.08.005

Deng, H., Poonoosamy, J., & Molins, S. (2022). A reactive transport modeling perspective on the dynamics of interface-coupled dissolution-precipitation. *Applied Geochemistry*, *137*, 105207. https://doi.org/10.1016/j.apgeochem.2022.105207

Deng, H., Tournassat, C., Molins, S., Claret, F., & Steefel, C. I. (2021). A pore-scale investigation of mineral precipitation driven diffusivity change at the column-scale. *Water Resources Research*, *57*(5), e2020WR028483. https://doi.org/10.1029/2020WR028483

De Windt, L., & Spycher, N. F. (2019). Reactive transport modeling: A key performance assessment tool for the geologic disposal of nuclear waste. *Elements*, *15*(2), 99–102. https://doi.org/10.2138/gselements.15.2.99

Emmanuel, S., & Ague, J. J. (2009). Modeling the impact of nano-pores on mineralization in sedimentary rocks. *Water Resources Research*, *45*(4), W04406. https://doi.org/10.1029/2008WR007170

Everall, N. J. (2010). Confocal Raman microscopy: Common errors and artefacts. *Analyst*, *135*(10), 2512–2522. https://doi.org/10.1039/C0AN00371A

Fukatsu, Y., Van Loon, L., Shafizadeh, A., Grolimund, D., Ikeda, Y., & Tsukahara, T. (2017). Effect of celestite precipitation in compacted illite on the diffusion of HTO, 36 Cl^-, and 22 Na^+. *Energy Procedia*, *131*, 133–139. https://doi.org/10.1016/j.egypro.2017.09.450

Hommel, J., Coltman, E., & Class, H. (2018). Porosity-permeability relations for evolving pore space: A review with a focus on (bio-)geochemically altered porous media. *Transport in Porous Media*, *124*(2), 589–629. https://doi.org/10.1007/s11242-018-1086-2

Hunt, A. G. (2004). Continuum percolation theory and Archie's law. *Geophysical Research Letters*, *31*(19), L19503. https://doi.org/10.1029/2004GL020817

Katz, G. E., Berkowitz, B., Guadagnini, A., & Saaltink, M. W. (2011). Experimental and modeling investigation of multicomponent reactive transport in porous media. *Journal of Contaminant Hydrology*, *120–121*, 27–44. https://doi.org/10.1016/j.jconhyd.2009.11.002

Kim, D., Mahabadi, N., Jang, J., & van Paassen, L. A. (2020). Assessing the kinetics and pore-scale characteristics of biological calcium carbonate precipitation in porous media using a microfluidic chip experiment. *Water Resources Research*, *56*(2), e2019WR025420. https://doi.org/10.1029/2019WR025420

Kulenkampff, J., Stoll, M., Gründig, M., Mansel, A., Lippmann-Pipke, J., & Kersten, M. (2018). Time-lapse 3D imaging by positron emission tomography of Cu mobilized in a soil column by the herbicide MCPA. *Scientific Reports*, *8*(1), 7091. https://doi.org/10.1038/s41598-018-25413-9

Lasaga, A. C. (1979). The treatment of multi-component diffusion and ion pairs in diagenetic fluxes. *American Journal of Science*, *279*(3), 324–346. https://doi.org/10.2475/ajs.279.3.324

Marty, N. C. M., Tournassat, C., Burnol, A., Giffaut, E., & Gaucher, E. C. (2009). Influence of reaction kinetics and mesh refinement on the numerical modelling of concrete/clay interactions. *Journal of Hydrology*, *364*(1), 58–72. https://doi.org/10.1016/j.jhydrol.2008.10.013

Masoudi, M., Fazeli, H., Miri, R., & Hellevang, H. (2021). Pore scale modeling and evaluation of clogging behavior of salt crystal aggregates in CO_2-rich phase during carbon storage. *International Journal of Greenhouse Gas Control*, *111*, 103475. https://doi.org/10.1016/j.ijggc.2021.103475

Menke, H. P., Maes, J., & Geiger, S. (2021). Upscaling the porosity–permeability relationship of a microporous carbonate for Darcy-scale flow with machine learning. *Scientific Reports*, *11*(1), 2625. https://doi.org/10.1038/s41598-021-82029-2

Mon, A., Samper, J., Montenegro, L., Naves, A., & Fernández, J. (2017). Long-term non-isothermal reactive transport model of compacted bentonite, concrete and corrosion products in a HLW repository in clay. *Journal of Contaminant Hydrology*, *197*, 1–16. https://doi.org/10.1016/j.jconhyd.2016.12.006

Noiriel, C., & Soulaine, C. (2021). *Pore-scale imaging and modelling of reactive flow in evolving porous media: Tracking the dynamics of the fluid–rock interface* (p. 140). Transport in Porous Media. https://doi.org/10.1007/s11242-021-01613-2

Noiriel, C., Steefel, C. I., Yang, L., & Ajo-Franklin, J. (2012). Upscaling calcium carbonate precipitation rates from pore to continuum scale. *Chemical Geology*, *318–319*, 60–74. https://doi.org/10.1016/j.chemgeo.2012.05.014

Noiriel, C., Steefel, C. I., Yang, L., & Bernard, D. (2016). Effects of pore-scale precipitation on permeability and flow. *Advances in Water Resources*, *95*, 125–137. https://doi.org/10.1016/j.advwatres.2015.11.013

Nooraiepour, M., Masoudi, M., & Hellevang, H. (2021). Probabilistic nucleation governs time, amount, and location of mineral precipitation and geometry evolution in the porous medium. *Scientific Reports*, *11*(1), 16397. https://doi.org/10.1038/s41598-021-95237-7

Poonoosamy, J., Curti, E., Kosakowski, G., Grolimund, D., Loon, L. R. V., & Mäder, U. (2016). Barite precipitation following celestite dissolution in a porous medium: A SEM/BSE and μ-XRD/XRF study. *Geochimica et Cosmochimica Acta*, *182*, 131–144. https://doi.org/10.1016/j.gca.2016.03.011

Poonoosamy, J., Klinkenberg, M., Deissmann, G., Brandt, F., Bosbach, D., Mäder, U., & Kosakowski, G. (2020). Effects of solution supersaturation on barite precipitation in porous media and consequences on permeability: Experiments and modelling. *Geochimica et Cosmochimica Acta*, *270*, 43–60. https://doi.org/10.1016/j.gca.2019.11.018

Poonoosamy, J., Kosakowski, G., Loon, L. R. V., & Mäder, U. (2015). Dissolution–precipitation processes in tank experiments for testing numerical models for reactive transport calculations: Experiments and modelling. *Journal of Contaminant Hydrology*, *177*(178), 1–17. https://doi.org/10.1016/j.jconhyd.2015.02.007

Poonoosamy, J., Lu, R., Lönartz, M. I., Deissmann, G., Bosbach, D., & Yang, Y. (2022). A lab on a chip experiment for upscaling diffusivity of evolving porous media. *Energies*, *15*(6), 2160. https://doi.org/10.3390/en15062160

Poonoosamy, J., Mahrous, M., Curti, E., Bosbach, D., Deissmann, G., Churakov, S., et al. (2021). A lab-on-a-chip approach integrating in-situ characterization and reactive transport modelling diagnostics to unravel (Ba, Sr)SO_4 oscillatory zoning. *Scientific Reports*, *11*(1), 23678. https://doi.org/10.1038/s41598-021-02840-9

Poonoosamy, J., Westerwalbesloh, C., Deissmann, G., Mahrous, M., Curti, E., Churakov, S., et al. (2019). A microfluidic experiment and pore scale modelling diagnostics for assessing mineral precipitation and dissolution in confined spaces. *Chemical Geology*, *528*, 119264. https://doi.org/10.1016/j.chemgeo.2019.07.039

Prasianakis, N. I., Haller, R., Mahrous, M., Poonoosamy, J., Pfingsten, W., & Churakov, S. V. (2020). Neural network based process coupling and parameter upscaling in reactive transport simulations. *Geochimica et Cosmochimica Acta*, *291*, 126–143. https://doi.org/10.1016/j.gca.2020.07.019

Prieto, M. (2014). Nucleation and supersaturation in porous media (revisited). *Mineralogical Magazine*, *78*(6), 1437–1447. https://doi.org/10.1180/minmag.2014.078.6.11

Putnis, A. (2015). Transient porosity resulting from fluid–mineral interaction and its consequences. *Reviews in Mineralogy and Geochemistry*, *80*(1), 1–23. https://doi.org/10.2138/rmg.2015.80.01

Rajyaguru, A., L'Hôpital, E., Savoye, S., Wittebroodt, C., Bildstein, O., Arnoux, P., et al. (2018). Experimental characterization of coupled diffusion reaction mechanisms in low permeability chalk. *Chemical Geology*, *503*, 29–39. https://doi.org/10.1016/j.chemgeo.2018.10.016

Rathnaweera, T. D., Ranjith, P. G., & Perera, M. S. A. (2016). Experimental investigation of geochemical and mineralogical effects of CO_2 sequestration on flow characteristics of reservoir rock in deep saline aquifers. *Scientific Reports*, *6*(1), 19362. https://doi.org/10.1038/srep19362

Roman, S., Poonoosamy, J., & Soulaine, C. (2020). A combination of microfluidics experiments and numerical simulations for the study of mineral reactivity at the pore-scale. Retrieved from https://juser.fz-juelich.de/record/888789

Sabo, M. S., & Beckingham, L. E. (2021). Porosity-permeability evolution during simultaneous mineral dissolution and precipitation. *Water Resources Research*, *57*(6), e2020WR029072. https://doi.org/10.1029/2020WR029072

Sahimi, M. (1994). *Applications of percolation theory* (1st ed.). CRC Press. https://doi.org/10.1201/9781482272444

Samper, J., Naves, A., Montenegro, L., & Mon, A. (2016). Reactive transport modelling of the long-term interactions of corrosion products and compacted bentonite in a HLW repository in granite: Uncertainties and relevance for performance assessment. *Applied Geochemistry*, *67*, 42–51. https://doi.org/10.1016/j.apgeochem.2016.02.001

Scheibe, T. D., Murphy, E. M., Chen, X., Rice, A. K., Carroll, K. C., Palmer, B. J., et al. (2015). An analysis platform for multiscale hydrogeologic modeling with emphasis on hybrid multiscale methods. *Groundwater*, *53*(1), 38–56. https://doi.org/10.1111/gwat.12179

Schindelin, J., Arganda-Carreras, I., Frise, E., Kaynig, V., Longair, M., Pietzsch, T., et al. (2012). Fiji: An open-source platform for biological-image analysis. *Nature Methods*, *9*(7), 676–682. https://doi.org/10.1038/nmeth.2019

Schovsbo, N. H., Holmslykke, H. D., Kjøller, C., Hedegaard, K., Kristensen, L., Thomsen, E., & Esbensen, K. H. (2016). Types of formation water and produced water in Danish oil-and gasfields: Implications for enhanced oil recovery by 'smart' water injection. *GEUS Bulletin*, *35*, 43–46. https://doi.org/10.34194/geusb.v35.4924

Seigneur, N., Mayer, K. U., & Steefel, C. I. (2019). Reactive transport in evolving porous media. *Reviews in Mineralogy and Geochemistry*, *85*(1), 197–238. https://doi.org/10.2138/rmg.2019.85.7

Shao, H., Kosakowski, G., Berner, U. R., Kulik, D. A., Mäder, U. K., & Kolditz, O. (2013). Reactive transport modeling of the clogging process at Maqarin natural analogue site. *Physics and Chemistry of the Earth*, *64*, 21–31. https://doi.org/10.1016/j.pce.2013.01.002

Soulaine, C., Gjetvaj, F., Garing, C., Roman, S., Russian, A., Gouze, P., & Tchelepi, H. A. (2016). The impact of sub-resolution porosity of x-ray microtomography images on the permeability. *Transport in Porous Media*, *113*(1), 227–243. https://doi.org/10.1007/s11242-016-0690-2

Soulaine, C., Roman, S., Kovscek, A., & Tchelepi, H. A. (2017). Mineral dissolution and wormholing from a pore-scale perspective. *Journal of Fluid Mechanics*, *827*, 457–483. https://doi.org/10.1017/jfm.2017.499

Steefel, C. I., & Lichtner, P. C. (1998). Multicomponent reactive transport in discrete fractures: II: Infiltration of hyperalkaline groundwater at Maqarin, Jordan, a natural analogue site. *Journal of Hydrology*, *209*(1), 200–224. https://doi.org/10.1016/S0022-1694(98)00173-5

Steefel, C. I., Molins, S., & Trebotich, D. (2013). Pore scale processes associated with subsurface CO_2 injection and sequestration. *Reviews in Mineralogy and Geochemistry*, *77*(1), 259–303. https://doi.org/10.2138/rmg.2013.77.8

Tang, Y., Valocchi, A. J., & Werth, C. J. (2015). A hybrid pore-scale and continuum-scale model for solute diffusion, reaction, and biofilm development in porous media. *Water Resources Research*, *51*(3), 1846–1859. https://doi.org/10.1002/2014WR016322

Tartakovsky, A., Redden, G., Lichtner, P., Scheibe, T., & Meakin, P. (2008). Mixing-induced precipitation: Experimental study and multiscale numerical analysis. *Water Resources Research*, *44*(6), W06S04. https://doi.org/10.1029/2006WR005725

Tartakovsky, A. M., Meakin, P., Scheibe, T. D., & Wood, B. D. (2007). A smoothed particle hydrodynamics model for reactive transport and mineral precipitation in porous and fractured porous media. *Water Resources Research*, *43*(5), W05437. https://doi.org/10.1029/2005WR004770

Tranter, M., De Lucia, M., & Kühn, M. (2021). Barite scaling potential modelled for fractured-porous geothermal reservoirs. *Minerals*, *11*(11), 1198. https://doi.org/10.3390/min11111198

Trinchero, P., Cvetkovic, V., Selroos, J.-O., Bosbach, D., & Deissmann, G. (2020). Upscaling of radionuclide transport and retention in crystalline rocks exhibiting micro-scale heterogeneity of the rock matrix. *Advances in Water Resources*, *142*, 103644. https://doi.org/10.1016/j.advwatres.2020.103644

Wagner, R., Kühn, M., Meyn, V., Pape, H., Vath, U., & Clauser, C. (2005). Numerical simulation of pore space clogging in geothermal reservoirs by precipitation of anhydrite. *International Journal of Rock Mechanics and Mining Sciences*, *42*(7–8), 1070–1081. https://doi.org/10.1016/j.ijrmms.2005.05.008

Wasch, L. J., Wollenweber, J., & Tambach, T. J. (2013). Intentional salt clogging: A novel concept for long-term CO2 sealing. *Greenhouse Gases: Science and Technology*, *3*(6), 491–502. https://doi.org/10.1002/ghg.1373

Xie, M., Mayer, K. U., Claret, F., Alt-Epping, P., Jacques, D., Steefel, C., et al. (2015). Implementation and evaluation of permeability-porosity and tortuosity-porosity relationships linked to mineral dissolution-precipitation. *Computational Geosciences*, *19*(3), 655–671. https://doi.org/10.1007/s10596-014-9458-3

Xie, M., Su, D., Mayer, K. U., & MacQuarrie, K. T. B. (2022). Reactive transport investigations of the long-term geochemical evolution of a multibarrier system including bentonite, low-alkali concrete and host rock. *Applied Geochemistry*, *143*, 105385. https://doi.org/10.1016/j.apgeochem.2022.105385

Xu, T., Senger, R., & Finsterle, S. (2008). Corrosion-induced gas generation in a nuclear waste repository: Reactive geochemistry and multiphase flow effects. *Applied Geochemistry*, *23*(12), 3423–3433. https://doi.org/10.1016/j.apgeochem.2008.07.012

Xu, T., Ontoy, Y., Molling, P., Spycher, N., Parini, M., & Pruess, K. (2004). Reactive transport modeling of injection well scaling and acidizing at Tiwi field, Philippines. *Geothermics*, *33*(4), 477–491. https://doi.org/10.1016/j.geothermics.2003.09.012

Zhang, C., Dehoff, K., Hess, N., Oostrom, M., Wietsma, T. W., Valocchi, A. J., et al. (2010). Pore-scale study of transverse mixing induced $CaCO_3$ precipitation and permeability reduction in a model subsurface sedimentary system. *Environmental Science & Technology*, *44*(20), 7833–7838. https://doi.org/10.1021/es1019788

References From the Supporting Information

Brooker, M. H., Hancock, G., Rice, B. C., & Shapter, J. (1989). Raman frequency and intensity studies of liquid H_2O, $H_2{}^{18}O$ and D_2O. *Journal of Raman Spectroscopy*, *20*(10), 683–694. https://doi.org/10.1002/jrs.1250201009

Chen, Y.-H., Huang, E., & Yu, S.-C. (2009). High-pressure Raman study on the $BaSO_4$-$SrSO_4$ series. *Solid State Communications*, *149*(45–46), 2050–2052. https://doi.org/10.1016/j.ssc.2009.08.023

Helgeson, H. C., Kirkham, D. H., & Flowers, G. C. (1981). Theoretical prediction of the thermodynamic behaviour of aqueous electrolytes at high pressures and temperatures: IV. Calculation of activity coefficients, osmotic coefficients, and apparent molal and standard and relative partial molal properties to 600°C and 5 kb. *American Journal of Science*, *281*(10), 1249–1516. https://doi.org/10.2475/ajs.281.10.1249

Kulik, D. A., Wagner, T., Dmytrieva, S. V., Kosakowski, G., Hingerl, F. F., Chudnenko, K. V., & Berner, U. R. (2013). GEM-Selektor geochemical modeling package: Revised algorithm and GEMS3K numerical kernel for coupled simulation codes. *Computational Geosciences*, *17*, 1–24. https://doi.org/10.1007/s10596-012-9310-6

Thoenen, T., Hummel, W., Berner, U., & Curti, E. (2014). *The PSI/Nagra chemical thermodynamic database 12/07*. Nagra Arbeitsbericht NAB 14-49.

Wagner, T., Kulik, D. A., Hingerl, F. F., & Dmytrieva, S. V. (2012). GEM-Selektor geochemical modeling package: TSolMod library and data interface for multicomponent phase models. *The Canadian Mineralogist*, *50*(5), 1173–1195. https://doi.org/10.3749/canmin.50.5.1173